4D IMAGING OF FLUID FLOW DYNAMICS IN NATURAL POROUS MEDIA WITH ULTRA-FAST X-RAY MICROTOMOGRAPHY

Souhail Youssef[1], Herve Deschamps[1], Jeremie Dautriat[1], Elisabeth Rosenberg[1], Rezki Oughanem[1-2], Eric Maire[2], Rajmund Mokso[3]
[1]IFP Energie nouvelles, [2] INSA-Lyon MATEIS CNRS UMR 5510, [3] Swiss Light Source, Paul Scherrer Institut,

This paper was prepared for presentation at the International Symposium of the Society of Core Analysts held in Napa Valley, California,, USA, 16-19 September, 2013.

ABSTRACT

We present preliminary results of 4D imaging of dynamic fluid flow in natural porous media. The experiment was conducted at the "Swiss Light Source" synchrotron facility taking advantage of the latest developments in ultra-fast microtomography at the TOMCAT beamline and of a specially designed setup to remotely control in-situ flow experiment. First we present the protocol of an imbibition experiment on a 5.8 mm diameter and 17% porosity sandstone sample. The 3D images were acquired with a voxel size of 5.5 µm and with a temporal resolution of 1s per 3D image. The resulting data sets are then processed to extract the mean saturation values and the saturation profiles along the sample as function of time. The captured images show 8 different stages of the imbibition process before the endpoint saturation is reached. This set of images is then segmented to extract local information such as the spatial distribution of trapped gas as a function of time and to analyze trapping mechanisms.

INTRODUCTION

Multiphase flow in natural porous media is central in a wide range of phenomena and applications in geosciences, including hydrocarbon formation and migration, oil and gas production, increased and enhanced oil recovery as well as CO_2 injection and sequestration. Over the past years, several models of fluid displacement mechanisms including fluid/fluid and fluid/solid interface descriptions have been proposed [1, 2] and integrated in numerical modeling schemes such as pore network models [3, 4]. The validation of such models is generally achieved either at the macroscopic level [5-7] or at the microscopic level using 2D glass micromodels [8]. Detailed experimental data of the 3D flow behavior at the microlevel have been studied in only few works in which systems with different saturation processes were imaged [9-12]. Nevertheless, the transient phenomena are rarely described in natural media. Moreover, the control of the equilibrium state clearly remains one of the major issues in imaging intermediate saturation states.

Recent developments in synchrotron based x-ray tomography [13] present an attractive alternative to overcome this limitation. Due to both the high photon flux of synchrotron radiation and a high speed camera, sub-second temporal resolution may be reached with a spatial resolution ranging from 2 to 20 µm. A miniaturized flow cell was specifically developed to perform in-situ computed microtomography (µCT) multiphase flow experiments, allowing a precise control of the experimental conditions (flow rate, pressure and temperature) [14].

In order to demonstrate the potential of this technique, this article focuses on spontaneous imbibition in dry sandstone. We will first describe the experimental setup. Then we will show the first quantitative information extracted from a series of 3D images captured during an imbibition test.

EXPERIMENTAL SETUP

Beamline and end-station configuration

The experiments were carried out at the TOMCAT beamline [15] at the Swiss Light Source where the x-ray source is a 2.9 T superbending magnet. The sample was exposed to a parallel polychromatic x-ray beam filtered to have a peak energy at around 25 keV. The polychromatic beam was chosen for several reasons: First it gives a high photon flux density allowing extremely short exposure times (1-2 ms); second it allows for 6 mm probing beam (compared to 3 mm for monochromatic beam); and, finally, by omitting the monochromator, high-frequency vibrations that can alter image qualities are avoided [13]. To shift the spectrum towards higher energies a 5% filter was used on the polychromatic beam. The transmitted x-ray was converted into visible light by a 100 µm LuAG scintillator and projected onto a high speed CMOS camera. The camera (pco.Dimax) is a 12-bit camera with 2016x2016 pixels and a physical pixel size of 11x11 µm². The image formed by the scintillator was projected at the detector sensor with a 2x magnification resulting in an image pixel size of 5.5 µm. The field of view was set to 1152x1152 pixels.

The acquisition conditions were set to 500 projections over 180°, with an exposure time of 2 ms in order to minimize acquisition times (1 s per 3D image) while keeping a satisfying image quality. As shown in [13], reducing the optimal number of projections (1800 for this setup) by a factor of four does not significantly affect the quality of reconstructed data. Figure 1 compares the same sample imaged with a standard laboratory µCT (acquisition time 150 min) and via the synchrotron facility using the aforementioned conditions (acquisition time 1 s). The corresponding gray level histograms are superimposed on the images. The images were acquired with the same pixel size. The quality of the images is comparable although the synchrotron-acquired image shows a histogram with a slightly broader distribution. We assume that such effect is mainly due to the phase contrast.

To achieve the dynamic image capture, the tomographic acquisition process was synchronized by allowing the rotation stage to rotate continuously at a constant speed calculated from the frame rate of the detector. The onboard RAM of the camera limits the

number of images to be acquired before pausing for image transfer to the reconstruction server. The chosen configuration allows for the acquisition of more than 15000 projections, i.e an acquisition interval of 30 s with a rate of one 3D image per second. Images were reconstructed using a Fourier transform-based tomographic reconstruction method which uses a prolate function for interpolation in the Fourier space [16].

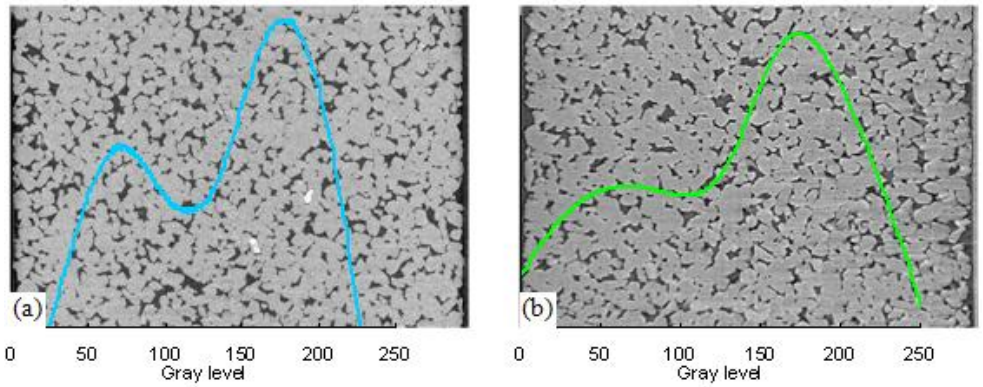

Figure 1. Comparison of tomographic images of Fontainebleau sandstone with 17% of porosity acquired with (a) standard laboratory µCT equipment in 150 min and (b) synchrotron facility captured in 1s. The curves overlaying the images represent a rescaled 8 bit gray level histogram.

Sample and imbibition experiment

The studied sample is a mini-core Fontainebleau sandstone from a block with a porosity of 17%. The mini-core has a diameter of 5.8 mm and a length of 8 mm. The dry sample was mounted in a PEEK core holder fixed on a rotation stage (the setup is illustrated in Figure 2). The bottom entry of the core holder is equipped with two downstream inlets, which allow sweeping the bottom face of the sample without forcing the injection of the fluid into the sample. The top face of the core remained open to air. One of the inlets was connected by flexible tubing to a HPLC type pump located outside of the experimental hutch. The distance separating the sample stage from the pump is approximately 10 m. The flexibility of the tubing allows the core holder to rotate continuously without inducing any tangential stress. The PEEK material ensures a good transparency to x-ray and a good mechanical stability.

The brine was prepared with 40 g/l KI to enhance the contrast between the brine and the air. Preliminary observations show that for this sample the spontaneous imbibition with water is very fast (less than a second). To slow down the water front velocity, the brine was viscosified by adding 65% by weight of glycerol leading to a viscosity of 15 cP.

As mentioned above the acquisition interval is 30s. The experiment begins with the initial acquisition of the radiographic images. After having insured the capture of at least one complete set of images of the sample, which will be considered as the ‘dry’ reference, the fluid is injected in the core holder at relatively high rate (0.2 cc/min). The flow rate was chosen to provide the sample with sufficient volume of brine to get a continuous and equilibrated spontaneous imbibition. The excess volume of fluid is released by the outlet of the cell (cf. Figure 2).

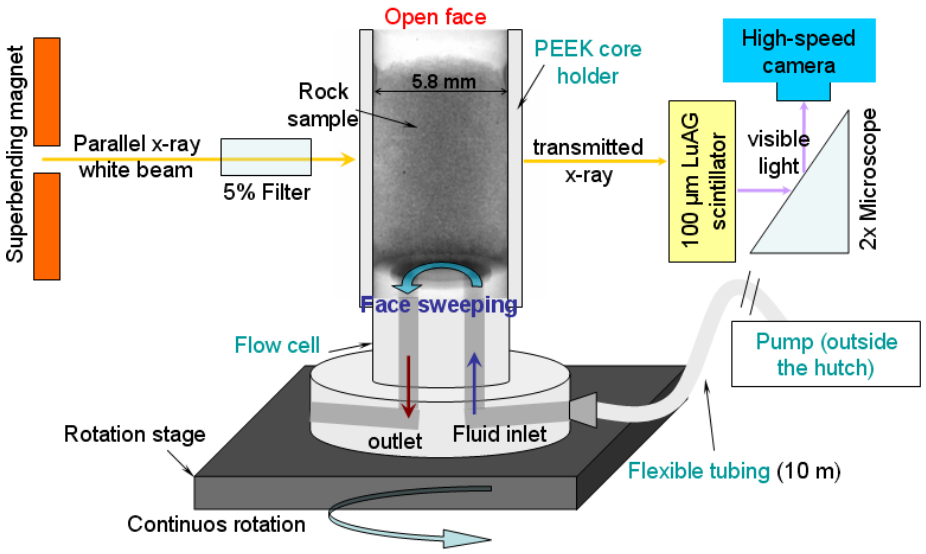

Figure 2. Setup for the dynamic flow imaging experiment, with sample core holder in synchrotron configuration beamline. The core holder is in sweeping configuration to allow spontaneous imbibition.

IMAGE PROCESSING

Figure 3(a) shows that the different phases can be qualitatively identified. However a straightforward segmentation is not possible due to the presence of some noise and gray level heterogeneities induced by the x-ray phase contrast. To reduce these effects, the image is first denoised by a mean filter (Figure 3(b)) and then a bilateral filter is used to homogenize the local gray level of each phase. Figure 3 summarizes the different steps of the filtering procedure and the resulting evolution of the histograms. The mean filter increases significantly the contrast between the three phases revealing three distinct peaks on the gray level histogram, whereas the bilateral filter leads to a more homogeneous gray level within each phase (Figure 3(c)).

Image processing is performed at three different length scales: the core scale, the local scale and the pore scale. Taking advantage of the coherence of the beam and the linear response of the detector, the mean brine saturation (S_b) of any given 3D image can be directly computed from its mean grey level using:

$$S_b = \frac{Mi - M_g}{M_b - M_g} \quad (1)$$

where M_i, M_b and M_g are the mean gray levels of respectively the partially saturated sample image, the 100% brine saturated sample image and the dry sample image.

In our case the reference image of the 100% brine saturation is not available. As the sample is mono-mineral, M_b can be calculated from the mean gray level of the three phases (gas, brine and mineral), as evaluated from the histogram peaks and noted respectively G_g, G_b and G_m. The image based porosity ϕ_{im} can be expressed as:

$$\phi_{im} = \frac{M_g - G_s}{G_g - G_s} = \frac{M_b - G_s}{G_b - G_s} \quad (2)$$

Combining both equations (1) and (2), the saturation is then expressed as a function of known parameters:

$$S_b = \frac{M_i - \phi_{im} G_g - (1-\phi_{im}) G_s}{\phi_{im}(G_b - G_g)} \quad (3)$$

In a similar way the mean saturation can be computed for each slice, allowing the calculation of saturation profiles in the flow direction.

In order to extract local information and statistical properties, the dry sample image was first segmented, and the pore space partitioned using the methodology described in [17]. A three phase histogram based segmentation [18] was then applied to each of the intermediate saturation images to extract the spatial distribution of the trapped phase.

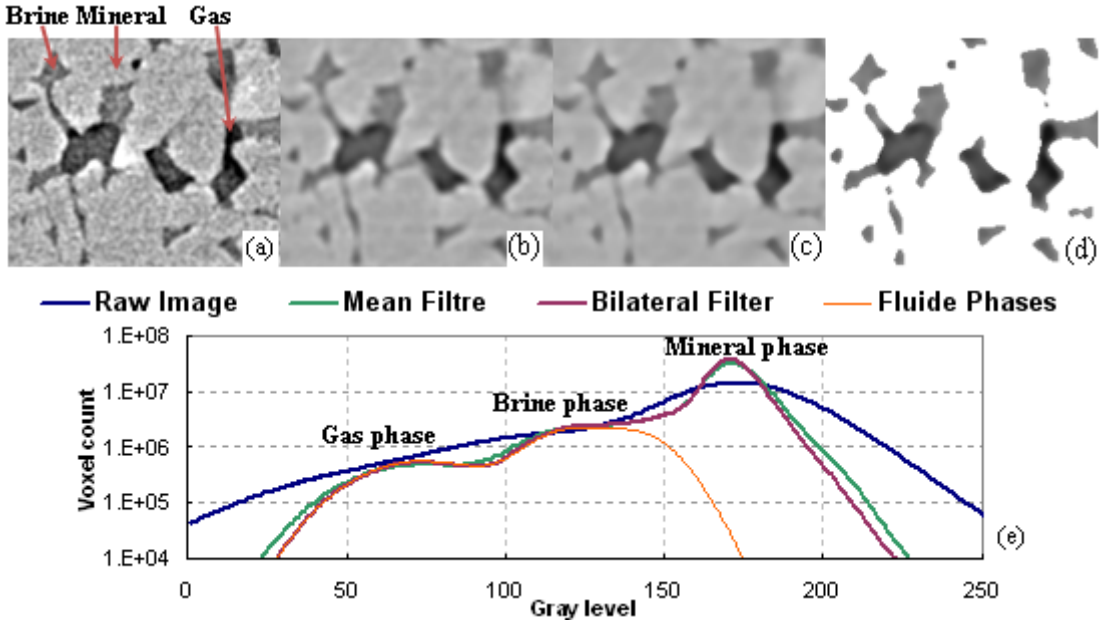

Figure 3. Image filtering steps: (a) raw images (b) mean filter (c) bilateral filter and (d) gas and brine phases and (e) the corresponding gray level histogram. The fluid phases image is obtained by image subtraction of the segmented dry sample image.

RESULTS

Figure 4 shows a series of 3D images for different time steps during the imbibition experiment. These images show the invasion of the brine phase (blue color) into the pore space (light red). During this invasion, gas bubbles are systematically trapped behind the fluid front (dark red). The first observation shows that images are free of motion artifacts and that the different phases are reasonably well resolved. By mean of this series of images we can state that the fluid displacement is very fast and that the imbibition of the region of 6 mm is completed in less than 8 s. Comparison of the image taken at 8 s and the one taken after 15 s shows no difference in the fluid distribution confirming the end

of the imbibition process. The gray level histograms of the first 8 s of the experiment are reported in Figure 5. We can distinguish three different zones corresponding to the three phases. The evolution in time of the histograms shows clearly a decrease of the gas peak compensated by an increase of the brine peak. Quantitative investigation was made at three different scales: the core scale, the local scale (corresponding to a 1D analyze of the saturation profile along the core) and the pore scale.

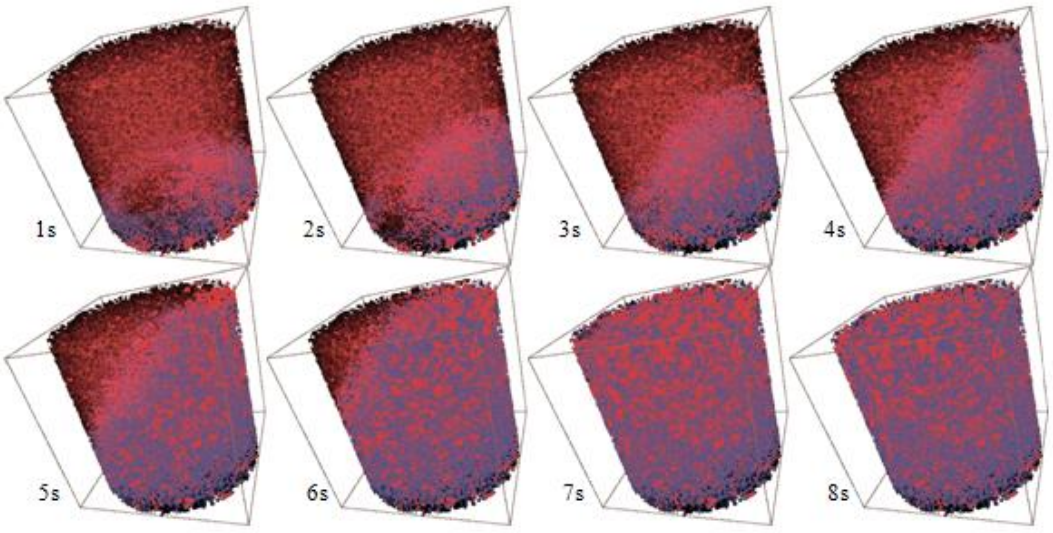

Figure 4. 3D images sequence of the imbibition process in a sandstone cylindrical sample with a porosity of 17% and a diameter of 5.8 mm. Successive images were taken with a time interval of 1 s and a voxel size of 5.5 µm. The mineral phase is represented in transparent light red, the brine in blue and the trapped gas in dark red.

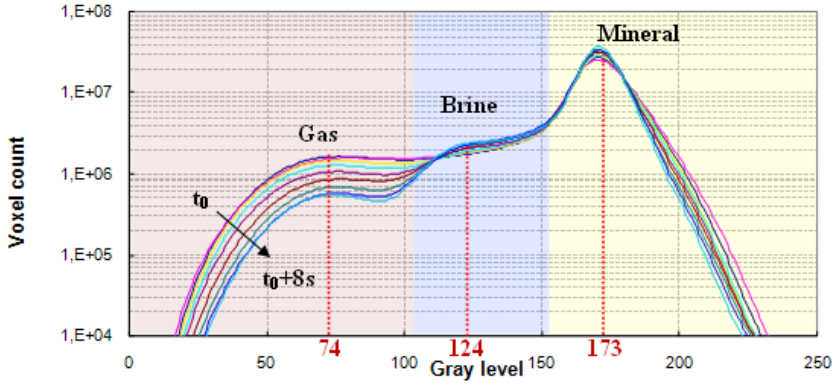

Figure 5. Gray level histogram evolution during the imbibition test.

This first qualitative description of the sequence of images acquired during the imbibition experiment shows that artifacts resulting from acquisition and/or reconstruction do not significantly affect the volumes, allowing visualization of the water front during imbibition. The increased viscosity of the invading fluid also appears to be necessary to obtain a coherent and exploitable data set, capable of a multi-scale quantitative description of the involved mechanisms.

Core scale investigation

First, the mean porosity of the dry sample image was computed. Porosity values of 16.4% and 15.8% were respectively obtained using equation (2) and the segmentation method [17]. Mean brine saturation was then calculated using equation (3) and plotted as a function of the square root of time in Figure 6. As qualitatively observed, this curve shows that the fluid saturation increases during the 8 s before it stabilizes at a value of 69%, corresponding to S_{rgw}. The saturation shows a linear dependence on the square root of time after the first 2 s of imbibition. This behavior is in accordance with the capillary rise behavior described by the Washburn equation. The imbibition rate (computed from the linear part of the curve) is 0.15 cc/min corresponding to a capillary number of $5\ 10^{-6}$.

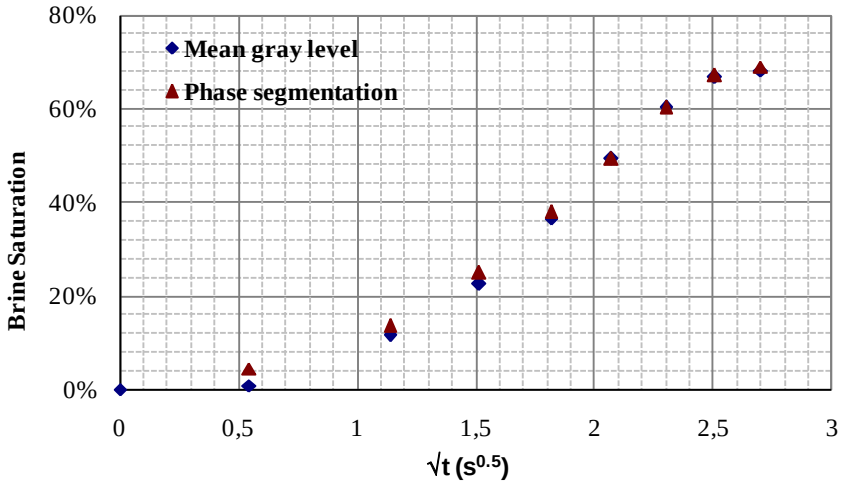

Figure 6. Evolution of water saturation in a 17% porosity sandstone by imbibition as function of the square root of time computed from 3D images.

Local scale investigation (1 D analyze)

At this scale, we consider the evolution of the fluid front propagation. For this purpose, the saturation is computed slice by slice in the direction of flow, using equation (3). From the bottom to the top, we are then able to build a saturation profile along the vertical direction for each 3D image. Figure 7 shows the evolution of the saturation profiles. Time interval between two profiles is 1 s. The two first profiles show that the entrance of the sample was partially saturated explaining the non-linearity observed at the beginning of the imbibition test. After 2 s the profiles became self-similar (i.e same shape) but with a smooth slope, indicating that the propagation fluid front is not sharp (in other words far from the ideal piston-like front model). This is confirmed in Figure 4 where we can see that the propagation front has an angle of approximately 45° with the vertical direction. This effect can be explained by a partial contact of the core entrance with the fluid at the first steps which results in an inclined front (cf. Figure 4 profile at 1 s). Nevertheless, the self similarity of the profiles indicates that the propagation front is homogeneous and that we are above the size of the representative elementary volume.

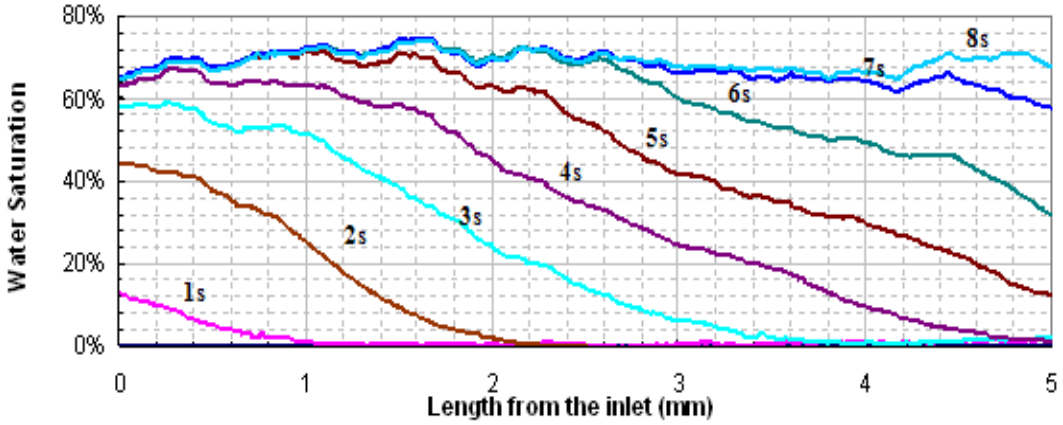

Figure 7. Saturation profiles along the 17% porosity sandstone sample with a time interval between each profile of 1 s.

Pore scale investigation

At this scale, the trapping gas mechanisms can be investigated. We consider a cropped volume from the segmented image to highlight the trapped gas phase. The considered sub-volume is presented in Figure 8. The image sequence shows that gas was trapped as small disconnected bubbles, in few pore bodies behind the brine front. Progression between two different states appears to be very quick (especially from 4 s to 6 s). In fact we observe almost 10% of saturation progress between the image taken at 4s and the one taken at 5s as indicated by Figure 6. Once the imbibition has reached the equilibrium state, the patches of trapped gas are homogeneously distributed along the sample and their shapes did not change any more.

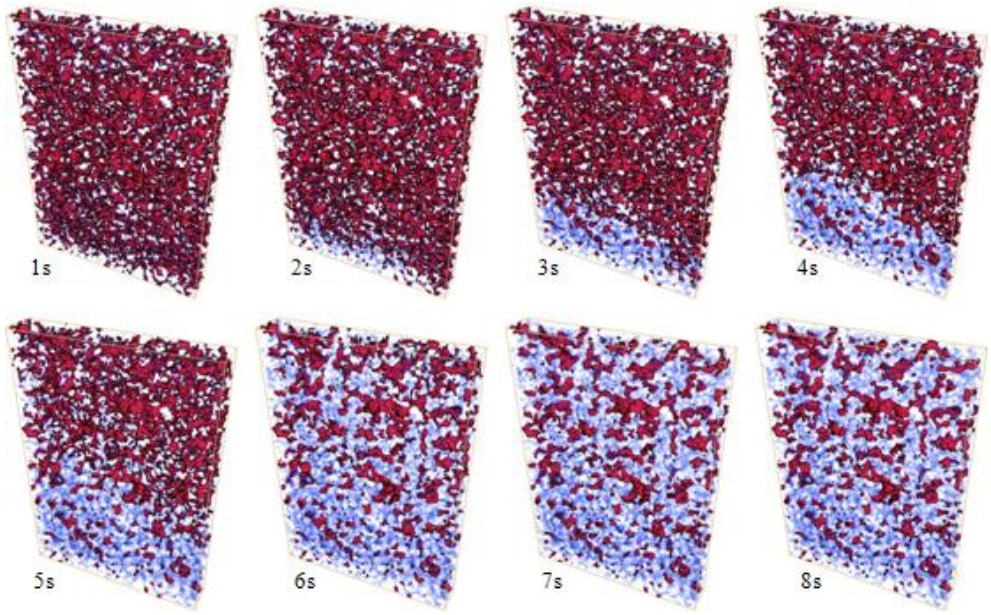

Figure 8. The 3D dynamic of trapped gas bubble generated by a spontaneous imbibition of 17% sandstone and captured by ultra-fast microtomography. Gas phase is in red and brine in blue.

To understand the impact of the local geometry on the trapped gas phase, we first extract the characteristics of the pore network from the image of the dry sample. Figure 9(a) shows the throat size and pore size distribution. The mean throat and pore radii are respectively 17.7 and 52.2 µm and the mean aspect ratio is equal to 4. Then, the pores containing gas are isolated at each time step. The distribution of this population of pore is reported Figure 9(b) for each time step (red curves). Finally the volume of gas trapped within each pore is computed and the distribution of the equivalent radius is reported in Figure 9(b) (blue curves). We can see that the shape of the distribution of the pore population that traps the gas as well as the local gas saturation does not change with time (cf. Figure 9(b)). This can explain the self similarity of the imbibition profiles. The mean radius of pores containing trapped gas is 60 µm which is higher than the mean pore radius of the sample. This confirms that gas is mainly trapped in the bigger pores.

The numerical and volume weighted distribution of trapped gas clusters (i.e connected gas component) are respectively presented in Figure 9(c) and Figure 9(d). The numerical distribution shows that the cluster size evolves towards larger sizes with time, which is more evidenced in the volume weighted distributions. This evolution might suggest a higher capillary pressure at the first step of the imbibition. Further investigations are needed to confirm this implication. The mean trapped gas cluster diameter at the equilibrium state is 51 µm, which is lower than the mean pore radius of the sample. This might suggest that the cluster is mainly trapped in single pores.

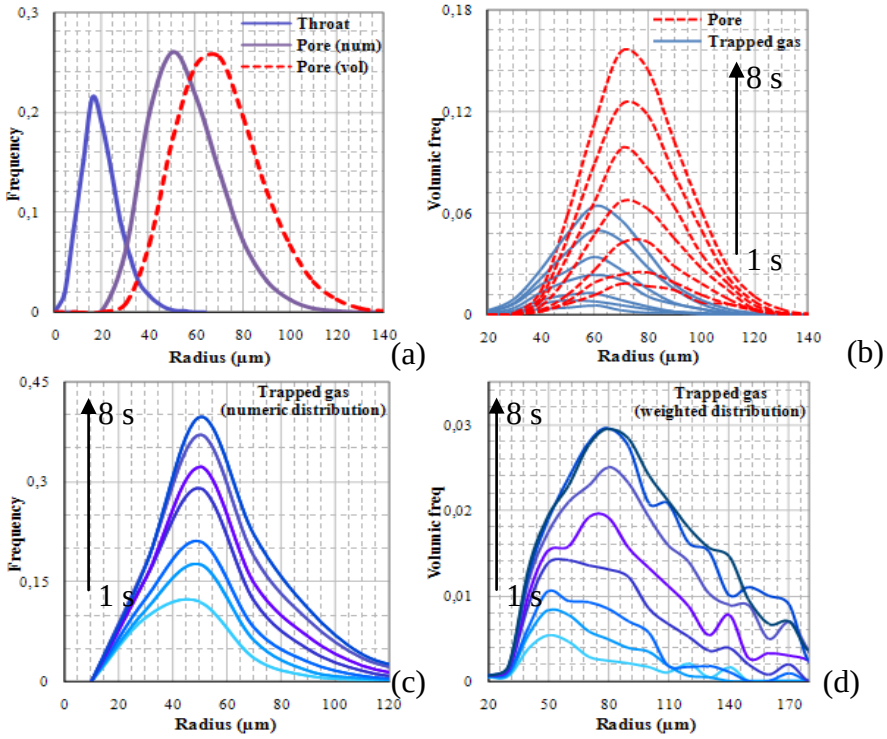

Figure 9. Pore network geometrical properties (a) and time evolution during the imbibition test of the trapping pore size (b) and trapped gas cluster size distribution (c) numeric distribution, (d) volume weighted distribution.

Local mechanisms

One of the aims of this work was to capture local mechanisms that govern the gas trapping phenomena. Figure 10 and Figure 11 show time series of 3D images at the pore scale. These sequences show the steps leading to the trapping of a gas cluster. We observe two different phenomena: water blocking and snap-off. Zones marked by an arrow indicate an incoming meniscus of water and those marked by a circle indicate a snap-off zone. We can see in Figure 10 that the brine is attempting to invade the central pore from all directions independently of the main flow direction. As all menisci reach the pore at almost the same moment, all paths allowing the gas to escape are blocked. In Figure 11 the gas cluster was trapped due to the interplay of the water blocking and snap-off. The water blocking results from the bypass of the neighboring pores (the left zone) that are rapidly invaded by the brine phase. The snap-off is observed far away from the brine meniscus (right zone) indicating the presence of precursor films. These observations suggest that the trapping phenomenon is triggered by the local (few pores) heterogeneity of the brine flow rate.

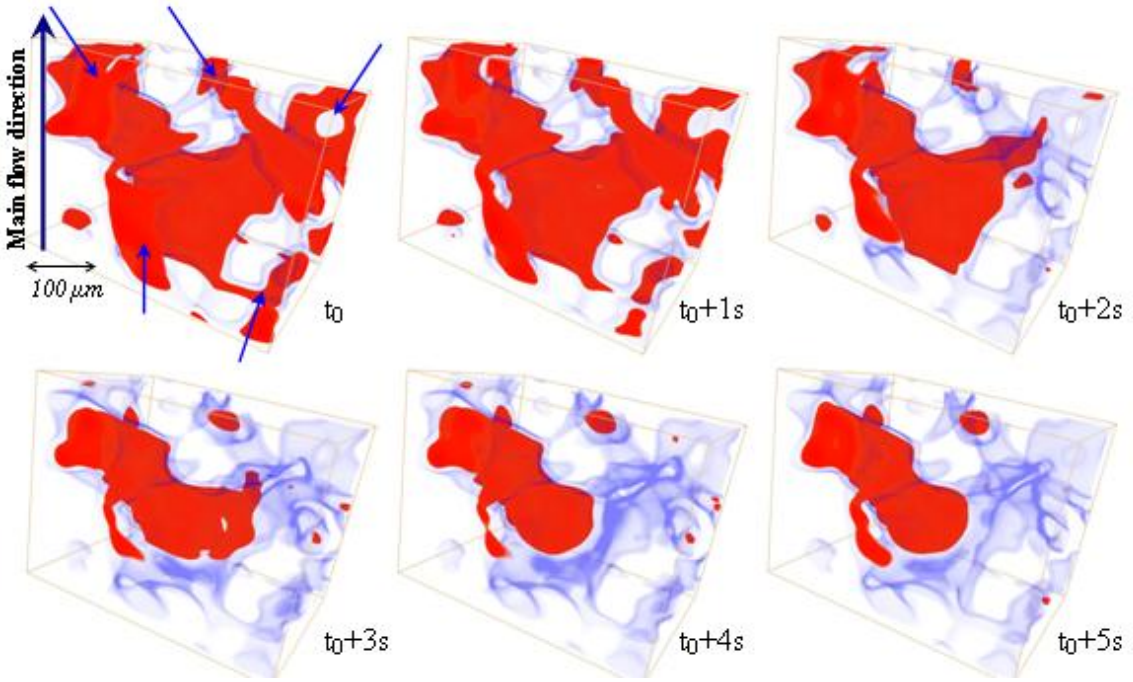

Figure 10 3D images time series of a trapping event during spontaneous imbibition with a time interval of 1 s and a resolution of 5.5 µm. Brine (in transparent blue) invades simultaneously the pore from all the pore throats (blue arrows) and blocks all the gas (in red) flow paths.

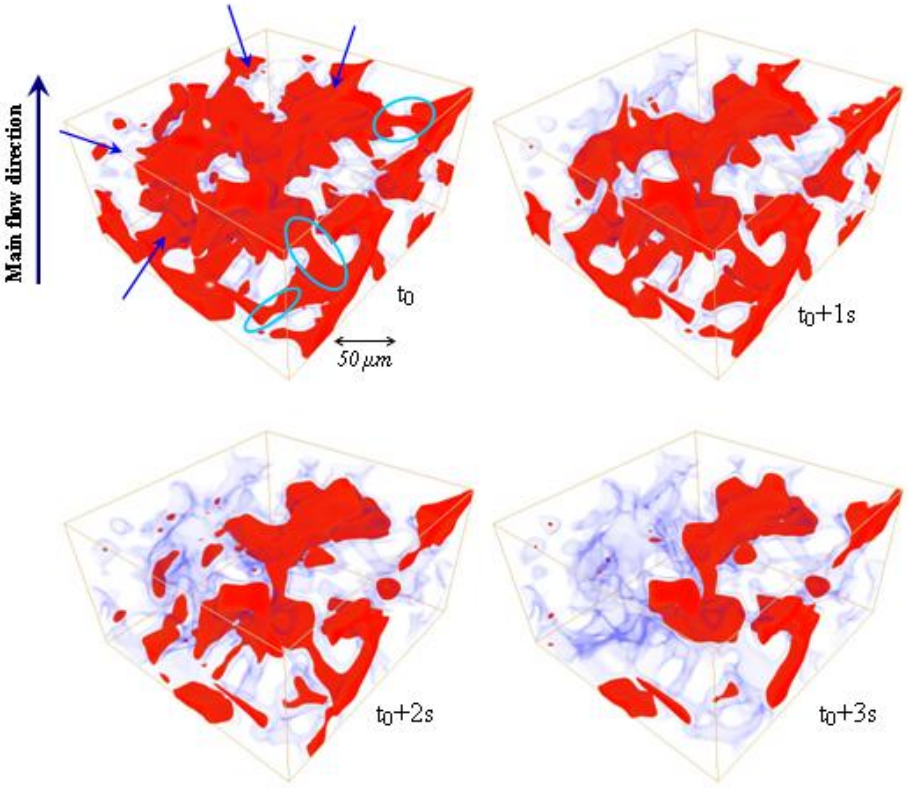

Figure 11. images time series of a trapping event during spontaneous imbibition with a time interval of 1s and a resolution of 5.5µm. Brine (in transparent blue) invades simultaneously the pore from the left side (blue arrows) while snap-off are occurring at the right side (circle) blocking all the gas (in red) flow path.

CONCLUSION

By combining the ultra-fast microtomography capability developed at the TOMCAT beam line and a dedicated in-situ experimental setup for fluid flow in porous media, we were able to follow a spontaneous imbibition in a sandstone with a voxel size of 5.5 µm and a temporal resolution of 1 s. Good quality images have allowed a quantitative description of the fluid invasion at different length scales giving valuable information on the trapping mechanisms. The saturation shows a linear dependence on the square root of time and a self-similar fluid front propagation. Gas clusters are mainly trapped in the biggest pores and the mechanisms that govern this trapping are mainly water blocking and snap-off. In a future work, more complex systems like oil/ water, surfactant and polymer injection will be investigated with this technique.

REFERENCES

1. Lenormand, R., C. Zarcone, and A. Sarr: "Mechanisms of the Displacement of One Fluid by Another in A Network of Capillary Ducts," *Journal of Fluid Mechanics* (1983), 337-353.
2. Chatzis, I. and F.A.L. Dullien: "Dynamic immiscible displacement mechanisms in pore doublet - Theory versus experiment," *Journal of Colloid and Interface Science* (1983), 199-222.

3. Blunt, M.J., M.D. Jackson, M. Piri, and P.H. Valvatne: "Detailed physics, predictive capabilities and macroscopic consequences for pore-network models of multiphase flow," *Advances in Water Resources* (2002), 1069-1089.
4. Joekar-Niasar, V., S.M. Hassanizadeh, and A. Leijnse: "Insights into the relationships among capillary pressure, saturation, interfacial area and relative permeability using pore-network modeling," *Transport in Porous Media* (2008), 201-219.
5. Bakke, S. and P.E. Oren: "3-D Pore-Scale Modelling of Sandstones and Flow Simulations in the Pore Networks," *Spe Journal* (1997), 136-149.
6. Knackstedt, M.A., C.H. Arns, A. Limaye, C.H. Arns, A. Limaye, A. Sakellariou, T.J. Senden, A.P. Sheppard, R.M. Sok, W.V. Pinczewski, and G.F. Bunn: "Digital core laboratory: Reservoir-core properties derived from 3D images," *Journal of Petroleum Technology* (2004), 66-68.
7. Laroche, C. and O. Vizika: "Two-phase flow properties prediction from small-scale data using pore-network modeling," *Transport in Porous Media* (2005), 77-91.
8. Lenormand, R., E. Touboul, and C. Zarcone: "Numerical models and experiments on immiscible displacements in porous media," *J Fluid Mech* (1988), 165-187.
9. Coles, M.E., R.D. Hazlett, P. Spanne, W.E. Soll, E.L. Muegge, and K.W. Jones: "Pore level imaging of fluid transport using synchrotron X-ray microtomography," *Journal of Petroleum Science and Engineering* (1998), 55-63.
10. Kumar, M. et al.: "Imaging of core scale distribution of fluids and wettability", *Int. Sym. of the Society of Core Analysts*, Abu Dhabi, UAE (2008) .
11. Prodanovic, M., W.B. Lindquist, and R.S. Seright: "3D image-based characterization of fluid displacement in a Berea core," *Advances in Water Resources* (2007), 214-226.
12. Seright, R.S., J. Liang, W.B. Lindquist, and J.H. Dunsmuir: "Characterizing disproportionate permeability reduction using synchrotron X-ray computed microtomography," *Spe Reservoir Evaluation & Engineering* (2002), 355-364.
13. Mokso, R. et al.: "Following Dynamic Processes by X-ray Tomographic Microscopy with Sub-second Temporal Resolution", *International Conference on X-ray Microscopy, AIP Conference Proceedings 1365,* (2011) ,38-41.
14. Youssef, S. et al.: "Towards a better understanding of Multiphase flow in porous media: 3D In-Situ fluid distribution imaging at the pore scale", *Int. Sym. of the Society of Core Analysts*, Noordwijk aan Zee, The Netherlands (2009) .
15. Stampanoni, M. et al.: "Trends in synchrotron-based tomographic imaging: the SLS experience", *Developments in X-Ray Tomography V, Proc. SPIE 6318*, (2006) .
16. Marone, F., B. Münch, and M. Stampanoni: "Fast reconstruction algorithm dealing with tomography artifacts", *Developments in X-Ray Tomography VII, Proc. SPIE 7804*, (2010) .
17. Youssef, S. et al.: "Quantitative 3D characterisation of the pore space of real rocks : improved µ-CT resolution and pore extraction methodology", *Int. Sym. of the Society of Core Analysts*, Calgary, Canada (2007) .
18. Bauer, D., S. Youssef, M. Han, S. Bekri, E. Rosenberg, M. Fleury, and O. Vizika: "From computed microtomography images to resistivity index calculations of heterogeneous carbonates using a dual-porosity pore-network approach: Influence of percolation on the electrical transport properties," *Physical review E* (1-7-2011), 011133